coatings

MDPI

*Article*

# Nanoengineering of Ultrathin Carbon-Coated T-$Nb_2O_5$ Nanosheets for High-Performance Lithium Storage

**Hualin Xiong [1,2,†], Changlong Du [1,2,†], Hongan Zhao [3], Lei Yu [1,2], Yongzhu Yan [1,2], Jinchuan Zhao [1,2,*], Gengping Wan [1,2,*], Liyong Wang [4,*] and Guizhen Wang [1,2]**

[1] Institute of Electromagnetic Protection Materials and Spectral Innovation Technology, State Key Laboratory of Tropic Ocean Engineering Materials and Materials Evaluation, School of Material Science and Engineering, Hainan University, Haikou 570228, China; 18094045563@163.com (H.X.); duchanglong@hainanu.edu.cn (C.D.); lei.yu@hainanu.edu.cn (L.Y.); yzyancam@hainanu.edu.cn (Y.Y.); wangguizhen0@hotmail.com (G.W.)

[2] Center for New Pharmaceutical Development and Testing of Haikou, Center for Advanced Studies in Precision Instruments, Haikou 570228, China

[3] China Academy of Space Technology (Xi'an), Xi'an 710100, China; horm1990@163.com

[4] School of Energy and Power Engineering, North University of China, Taiyuan 030001, China

* Correspondence: zhaojinchuan@hainanu.edu.cn (J.Z.); wangengping001@163.com (G.W.); nucc@nuc.edu.cn (L.W.)

† These authors contributed equally to this work.

**Abstract:** Niobium pentoxide ($Nb_2O_5$) is a promising anode candidate for lithium-ion batteries due to its high theoretical capacity, excellent rate capability, and safe working potential. However, its inherent low conductivity limits its practical application in fast-charging scenarios. In this work, we develop an ultrathin carbon-coated two-dimensional T-$Nb_2O_5$ nanosheet composite (T-$Nb_2O_5$@UTC) through a facile solvothermal reaction and subsequent CVD acetylene decomposition. This unique design integrates a two-dimensional nanosheet structure with an ultrathin carbon layer, significantly enhancing electronic conductivity, reducing ion diffusion pathways, and preserving structural integrity during cycling. The T-$Nb_2O_5$@UTC electrode demonstrates an impressive specific capacity of 214.7 mAh $g^{-1}$ at a current density of 0.1 A $g^{-1}$, maintaining 117.9 mAh $g^{-1}$ at 5 A $g^{-1}$, much outperforming the bare T-$Nb_2O_5$ (179.6 mAh $g^{-1}$ at 0.1 A $g^{-1}$ and 62.9 mAh $g^{-1}$ at 5 A $g^{-1}$). It exhibits outstanding cyclic stability, retaining a capacity of 87.9% after 200 cycles at 0.1 A $g^{-1}$ and 83.7% after 1000 cycles at 1 A $g^{-1}$. In a full-cell configuration, the assembled T-$Nb_2O_5$@UTC||$LiFePO_4$ battery exhibits a desirable specific capacity of 186.2 mAh $g^{-1}$ at 0.1 A $g^{-1}$ and only a 1.5% capacity decay after 120 cycles. This work underscores a nanostructure engineering strategy for enhancing the electrochemical performance of $Nb_2O_5$-based anodes toward high-energy-density and fast-charging applications.

**Keywords:** T-$Nb_2O_5$; carbon coating; rate performance; lithium-ion batteries; cycling stability

Academic Editor: Torsten Brezesinski

Received: 4 February 2025
Revised: 27 February 2025
Accepted: 6 March 2025
Published: 7 March 2025

**Citation:** Xiong, H.; Du, C.; Zhao, H.; Yu, L.; Yan, Y.; Zhao, J.; Wan, G.; Wang, L.; Wang, G. Nanoengineering of Ultrathin Carbon-Coated T-$Nb_2O_5$ Nanosheets for High-Performance Lithium Storage. *Coatings* **2025**, *15*, 315. https://doi.org/10.3390/coatings15030315

## 1. Introduction

With the increasing demand for high-energy-density and fast-charging energy storage devices in modern society, the development of advanced anode materials with superior rate performance and cycling stability has become a research hotspot for lithium-ion batteries (LIBs)s [1–3]. Traditional graphite anode materials are widely used due to their relatively high specific capacity (372 mAh $g^{-1}$) and excellent electrical conductivity, but their limited lithium-ion diffusion kinetics and poor rate performance restrict their application in fast-charging batteries [4,5]. Silicon-based anodes have an extremely high theoretical specific capacity (~4200 mAh $g^{-1}$), but they typically suffer severe volume expansion (~300%) during the Li-ion insertion and extraction processes, resulting in electrode structure collapse and rapid capacity degradation. This volume effect limits the practicality of silicon-based anodes in high-energy-density and long-cycle-life applications. Therefore, there is a pressing need to explore novel anode materials that can maintain excellent cycling stability while achieving higher rate performance. Among the emerging candidates, niobium pentoxide ($Nb_2O_5$) has attracted considerable attention as an intercalation-type transition metal oxide anode with fast pseudocapacitive $Li^+$ storage, high structural stability, and a safe working potential (above 1.0 V vs. $Li/Li^+$) that avoids lithium dendrite growth and solid electrolyte interphase formation [6–10]. Especially, the layered open framework structures of orthorhombic T-phase $Nb_2O_5$ provide rapid ion transport channels along the (001) plane during lithium insertion/extraction [11,12]. However, the unoccupied $d^0$ electronic configuration of $Nb^{5+}$ in $Nb_2O_5$ renders it a semiconductor with a wide bandgap (4 eV). Its relatively poor electrical conductivity ($3 \times 10^{-6}$ S $cm^{-1}$ at 300 K) still limits its practical application in high-energy-density and fast-charging scenarios [13–15].

To address this challenge, nanostructure engineering has been considered a promising approach to improve the electrical conductivity and enhance the electrochemical performance of T-$Nb_2O_5$ [16,17]. In particular, the two-dimensional (2D) nanosheet structure design exhibits several key advantages for electrode materials. It can significantly shorten the electron and ion diffusion pathways and offer a larger surface area for lithium-ion insertion [18,19]. Not only that, it facilitates better contact with conductive additives, which further improves the electrical conductivity of the material [20]. By leveraging these benefits, 2D T-$Nb_2O_5$ nanosheets can effectively mitigate the limitations of traditional bulk materials in electrochemical applications. In addition, carbon coating has been demonstrated to be an effective surface engineering scheme that can simultaneously enhance bulk electron transport and mitigate structural degradation throughout electrochemical cycling, thereby achieving a synergistic enhancement of capacity retention and initial coulombic efficiency [21]. Therefore, the choice of coating technology is crucial to the uniformity, thickness control, and interfacial bonding of the carbon layer, factors that are particularly critical for 2D nano systems. Traditional methods such as hydrothermal carbonization and sol–gel coating usually result in uneven carbon deposition (thickness variation > 5 nm) or pore blockage caused by precursor infiltration [22,23], which significantly reduces the accessible surface area of 2D nanosheets. In contrast, chemical vapor deposition (CVD) can precisely control the carbon layer at the nanoscale, achieving ultra-thin thickness-controlled conformal coating while retaining the 2D morphology, which is particularly suitable for composite material design [24–26]. Hence, combining the nanostructure design and surface modification is expected to synergistically improve the electrochemical performance of T-$Nb_2O_5$, providing a pathway to achieving high energy density, excellent rate capability, and enhanced cycling stability in LIBs.

In this study, we present the synthesis of a two-dimensional T-$Nb_2O_5$ nanosheet coated with an ultrathin carbon (UTC) layer (thickness < 5 nm) composite (T-$Nb_2O_5$@UTC) through a straightforward solvothermal reaction followed by CVD acetylene decomposition. The artful combination of the two-dimensional nanosheet structure and UTC coating aims to address the inherent limitations of T-$Nb_2O_5$ in terms of electrical conductivity and specific capacity, thereby significantly improving its electrochemical performance in LIBs. As a result, the T-$Nb_2O_5$@UTC electrode achieves remarkable pseudocapacitive lithium storage of 96.8% at 1.1 mV $s^{-1}$. The initial specific capacity can reach 214.7 mAh $g^{-1}$ at 0.1 A $g^{-1}$ and retain 117.9 mAh $g^{-1}$ at 5 A $g^{-1}$, much better than that of the bare T-$Nb_2O_5$ (179.6 mAh $g^{-1}$ at 0.1 A $g^{-1}$ and 62.9 mAh $g^{-1}$ at 5 A $g^{-1}$). Moreover, the T-$Nb_2O_5$@UTC exhibits outstanding cyclic stability, with 87.9% capacity retention after 200 cycles at 0.1 A $g^{-1}$ and 83.7% capacity retention after 1000 cycles at 1 A $g^{-1}$. When assembled with $LiFePO_4$, the full cell delivers a specific capacity of 186.2 mAh $g^{-1}$ at 0.1 A $g^{-1}$ and 98.5% capacity retention after 120 cycles. This work demonstrates a successful strategy for improving the electrochemical performance of T-$Nb_2O_5$ and provides valuable insights for developing advanced anode materials with high energy density and excellent rate capability for next-generation LIBs.

## 2. Results and Discussion

### *2.1. Preparation and Structural Characterization of T-$Nb_2O_5$@UTC*

The general preparation process of T-$Nb_2O_5$@UTC is illustrated in Figure 1a. Initially, a flake-like T-$Nb_2O_5$ precursor is synthesized using an isopropanol-based solvothermal reaction. The obtained precursor is then transferred to a muffle furnace and subjected to high-temperature annealing in an air atmosphere to convert it into T-$Nb_2O_5$. Subsequently, utilizing acetylene decomposition of chemical vapor deposition (CVD) achieves a uniform carbon coating on the T-$Nb_2O_5$ nanosheets. More synthesis details are reflected in the supporting information. Scanning electron microscopy (SEM) captures the real morphological changes of the T-$Nb_2O_5$ precursor, T-$Nb_2O_5$, and T-$Nb_2O_5$@UTC. As shown in Figure 1b, the T-$Nb_2O_5$ precursor presents a smooth two-dimensional sheet-like structure. After air calcination, the acquired T-$Nb_2O_5$ inherits this two-dimensional nanosheet structure of precursor well (Figure 1c). Moreover, it is noteworthy that a porous architecture develops between primary particles through the volatilization of organic constituents during high-temperature calcination processes. After the CVD process, no significant morphological changes are observed except for a slight decrease in pore size. This indicates that the carbon coating on the nanosheets has been successfully achieved (Figure 1d). The detailed structure of T-$Nb_2O_5$@UTC was investigated by means of transmission electron microscopy (TEM). Figure 1e shows a single T-$Nb_2O_5$@UTC sheet assembled from many primary nanoparticles. Figure 1f presents a further high-magnification TEM image of a single primary particle, where an UTC layer (less than 5 nm thick) is clearly visible on the particle surface. In addition, lattice fringes with a spacing of approximately 0.481 nm were obtained by fast Fourier transform (FFT), corresponding to the (060) crystal plane of T-$Nb_2O_5$ (Figure 1g). The elemental distribution mapping in Figure 1h further manifests that carbon (C) is uniformly distributed across the primary particles. These results verify the successful carbon encapsulation via the acetylene decomposition of CVD.

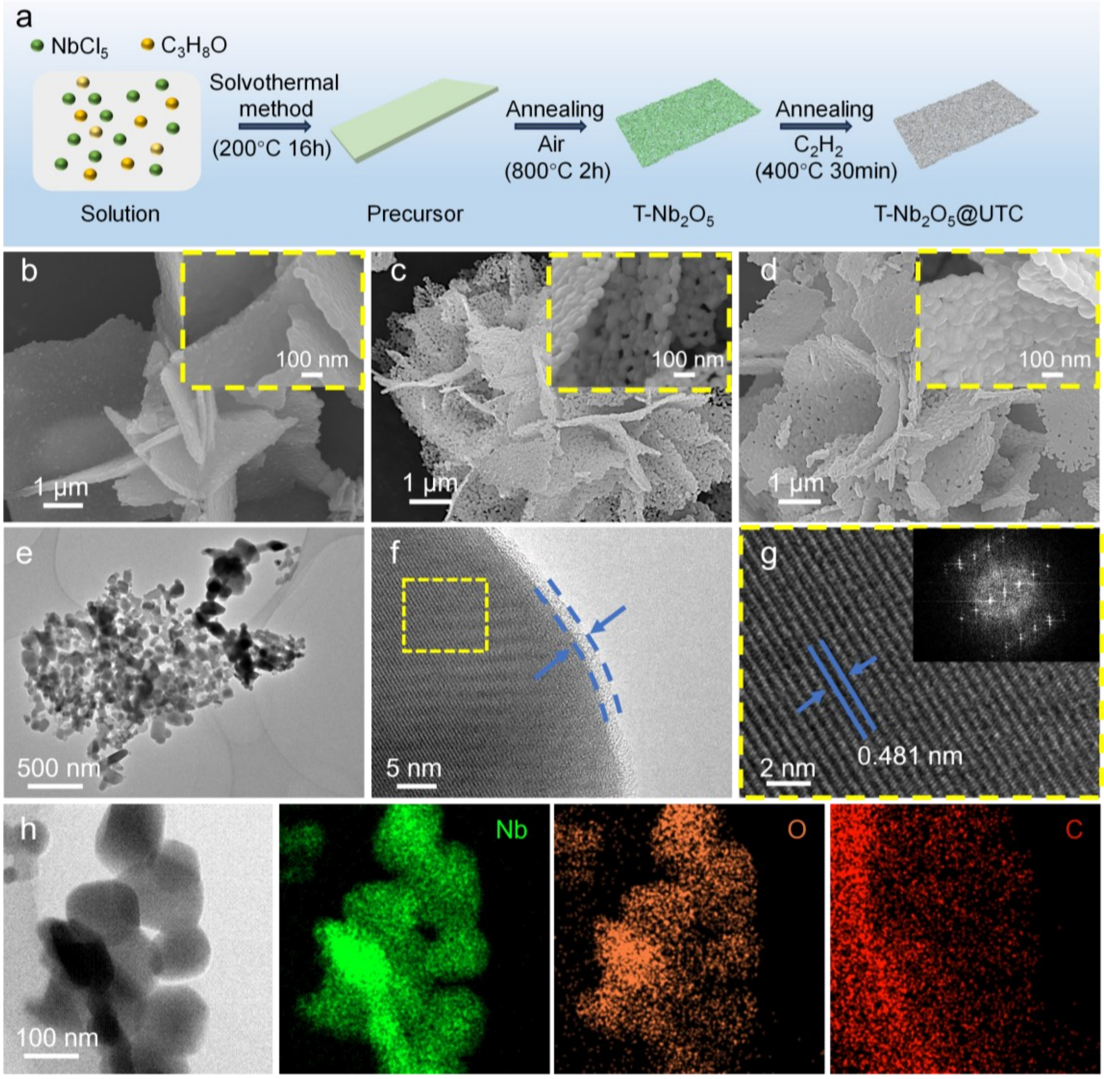

**Figure 1.** (**a**) The synthesis process of the T-$Nb_2O_5$@UTC. (**b**–**d**) SEM images of T-$Nb_2O_5$ precursor, T-$Nb_2O_5$, and T-$Nb_2O_5$@UTC. (**e**) TEM image of T-$Nb_2O_5$@UTC. (**f**,**g**) HRTEM images of T-$Nb_2O_5$@UTC. (**h**) EDS mapping images of T-$Nb_2O_5$@UTC.

### *2.2. Crystal Structure and Vibrational Analysis of T-$Nb_2O_5$ and T-$Nb_2O_5$@UTC*

XRD was utilized to detect the crystal structure of T-$Nb_2O_5$ and T-$Nb_2O_5$@UTC. As shown in Figure 2a, the diffraction peaks of these two samples are consistent with the standard card of T-$Nb_2O_5$ (JCPDS No. 27-1003), and the three strong peaks at 22.6°, 28.4°, and 36.6° correspond to the (001), (180), and (181) crystal planes of T-$Nb_2O_5$ [27], respectively. Notably, the lattice parameters of T-$Nb_2O_5$@UTC are a = 6.1784 Å, B = 29.2867 Å, c = 3.9286 Å, while the parameters of T-$Nb_2O_5$ are a = 6.1757 Å, B = 29.2966 Å, c = 3.9282 Å, respectively. This indicates that the carbon coating does not alter the crystal structure of T-$Nb_2O_5$ (Figure S1). The additional peaks at 22.5°, 31°, and 40° may be caused by the preferred orientation of the crystal plane during sample preparation or by weak signal interference or structural defects related to experimental conditions [28–30]. Since all the main diffraction peaks match the T-$Nb_2O_5$ standard card, the unassigned peaks do not affect the core conclusions of this article. Moreover, the XRD results indicate UTC coating does not alter the crystal structure of T-$Nb_2O_5$. The bonding vibrations between metal and oxygen were analyzed by means of Raman spectroscopy (Figure 2b). The characteristic peaks observed at 230 $cm^{-1}$ and 312 $cm^{-1}$ are associated with the bending vibrations of the Nb–O–Nb bond, whereas the peak at 690 $cm^{-1}$ is attributed to the symmetric stretching vibrations of $NbO_6$ and $NbO_7$ octahedra [31,32], respectively. The characteristic vibrational modes at 1350 and 1610 $cm^{-1}$ are attributed to the D and G bands, respectively, which are associated with disorder-induced carbon and the graphitic $sp^2$ carbon structure. The intensity ratio of these two bands (about 0.8) suggests that the carbon is partially graphitized while retaining some structural disorder [33]. Fourier transform infrared (FTIR) spectra were also recorded for these two samples (Figure 2c). The vibrational signatures observed at 1639 and 3452 $cm^{-1}$ are characteristic of O–H stretching modes, arising from surface-adsorbed atmospheric water molecules. Furthermore, the spectral features below 1000 $cm^{-1}$ originate from symmetric and asymmetric stretching vibrations within the Nb–O coordination framework [34].

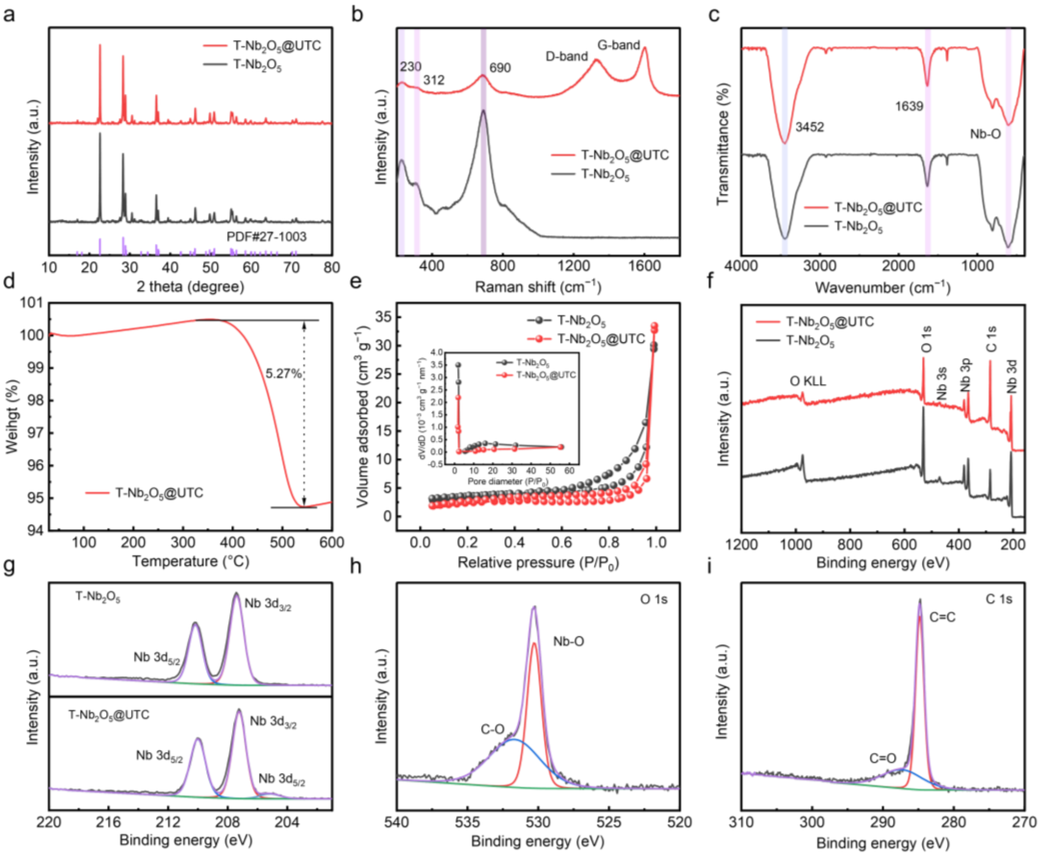

**Figure 2.** (**a**) XRD pattern of T-$Nb_2O_5$ and T-$Nb_2O_5$@UTC. (**b**) Raman spectra comparing T-$Nb_2O_5$ and T-$Nb_2O_5$@UTC. (**c**) FTIR curves of both materials. (**d**) Thermogravimetric (TG) curve of T-$Nb_2O_5$@UTC. (**e**) BET surface area curves. (**f**) XPS spectra for T-$Nb_2O_5$ and T-$Nb_2O_5$@UTC. XPS elemental spectra for (**g**) Nb, (**h**) O, and (**i**) C in T-$Nb_2O_5$@UTC.

### *2.3. Carbon Content and Surface Area Analysis of T-$Nb_2O_5$ and T-$Nb_2O_5$@UTC*

To determine the carbon coating content, thermogravimetric analysis (TGA) was conducted under an air atmosphere with a linear temperature ramp (10 °C $min^{-1}$) up to 600 °C to achieve controlled calcination (Figure 2d). The TG curve revealed that the weight content of carbon was 5.27%. Surface area measurements of T-$Nb_2O_5$@UTC and T-$Nb_2O_5$ were conducted using $N_2$ adsorption–desorption. As shown in Figure 2e, The Brunauer–Emmett–Teller (BET) surface areas were calculated as 8.3679 $m^2$ $g^{-1}$ for T-$Nb_2O_5$@UTC and 9.6568 $m^2$ $g^{-1}$ for T-$Nb_2O_5$. The slight decrease in specific surface area may be due to the filling of the mesoporous structure between nanoparticles by the ultrathin carbon layer (UTC), which makes some pores unable to be effectively adsorbed by $N_2$ molecules. These two samples exhibit abundant mesopores on their surfaces, and the pore size values are summarized in Table S1. Pore size distribution analysis indicates a predominant mesoporous range of 3–5 nm for both materials (Figure 2e, inset), in agreement with the morphological features observed by SEM. This porous structure facilitates the formation of multiple lithium-ion transport pathways, thereby enhancing ion mobility during electrochemical processes.

### *2.4. Elemental Composition and Chemical State Analysis by XPS*

X-ray photoelectron spectroscopy (XPS) analysis was performed to determine the elemental composition and chemical bonding states, with the corresponding survey spectra presented in Figure 2f. The enhancement of the C signal in T-$Nb_2O_5$@UTC is caused by surface carbon coating. The spin–orbit splitting resulted in the splitting of the Nb 3d peak into two components at about 207 and 210 eV with a peak area ratio of 3:2 (Figure 2g), confirming that $Nb^{5+}$ is the dominant oxidation state [35]. It is noteworthy that in T-$Nb_2O_5$@UTC, the $Nb^{5+}$ peak shifts 0.2 eV toward lower binding energy. This can be attributed to the electron transfer between the Nb, O, and C. The peak at 205.4 eV belongs to $Nb^{4+}$. This may be due to the fact that $H_2$ produced by the cracking of acetylene at high temperature reduces a small amount of $Nb_2O_5$ [36]. The O 1s peaks shown in Figure 2h appear at 530.22 and 531.82 eV, which can be attributed to Nb–O and C–O bonds [37,38], respectively. Additionally, the C 1s spectrum can be deconvoluted into two distinct peaks (Figure 2i), corresponding to C=C and C=O bonds [22]. These C-related bonds likely originate from the surface carbon layer. Both T-$Nb_2O_5$ and T-$Nb_2O_5$@UTC exhibit similar Nb and O atomic ratios, indicating that the UTC coating does not significantly alter the structural integrity of T-$Nb_2O_5$. Furthermore, a substantial increase in surface carbon content observed in T-$Nb_2O_5$@UTC confirms the success of the UTC coating (Table S2).

### *2.5. Electrochemical Performance Test*

We tested T-$Nb_2O_5$@UTC||Li and T-$Nb_2O_5$||Li cells to explore how the nanosheet structure and UTC coating influence lithium-ion storage capacity. Compared with T-$Nb_2O_5$, the first three cyclic voltammetry (CV) curves of T-$Nb_2O_5$@UTC remain almost unchanged (Figure 3a, d), confirming that the UTC coating can significantly enhance the electrochemical stability of T-$Nb_2O_5$ and inhibit the occurrence of side reactions. Furthermore, as the scan rate increased from 0.2 to 1.1 mV $s^{-1}$, the oxidation potential of T-$Nb_2O_5$@UTC shifted positively by 0.06 V, clearly superior to that of T-$Nb_2O_5$ (0.24 V) (Figure 3b, e). Compared with T-$Nb_2O_5$, the CV curve of T-$Nb_2O_5$@UTC features a larger area, suggesting a bigger energy storage capacity and fast reaction kinetics. This illustrates that UTC modification and a 2D nanosheet structure can effectively improve electrochemical reaction kinetics and reduce polarization effects.

To further investigate the effects of the 2D nanosheet structure and carbon encapsulation on electrochemical energy storage behavior, the relationship between the peak current ($i_p$) and the square root of the scan rate ($v^{0.5}$) in the CV curves of T-$Nb_2O_5$ and T-$Nb_2O_5$@UTC was analyzed (Figure 3c, f). The $i_p$ corresponding to the redox reactions of T-$Nb_2O_5$ and T-$Nb_2O_5$@UTC show a linear relationship with $v^{0.5}$ (Figure S2). Therefore, the electrochemical reactions of T-$Nb_2O_5$ and T-$Nb_2O_5$@UTC are diffusion-limited [39–41]. The reaction kinetics of T-$Nb_2O_5$ and T-$Nb_2O_5$@UTC were further studied by fitting the slope of the peak current (b value) with the scan rate using Eq S1. The b value theoretically lies between 0.5 and 1 and can serve as a quantitative indicator of the charge storage mechanism: values close to 1 indicate a predominantly capacitive behavior, whereas values close to 0.5 reflect a diffusion-controlled process. Specifically, the b-values for the oxidation reactions of T-$Nb_2O_5$@UTC and T-$Nb_2O_5$ are 0.976 and 0.936, and the b-values for the reduction reactions are 0.904 and 0.902, respectively. These values range from 0.5 to 1, indicating that the redox reactions of T-$Nb_2O_5$ and T-$Nb_2O_5$@UTC are synergistically controlled by surface capacitance and surface diffusion. We calculated the percentage contribution of capacitance to the total electrode capacity by Equation (S2). The capacitance contribution of T-$Nb_2O_5$@UTC increases from 92.7% to 96.8% as the scan rate rises from 0.2 to 1.1 mV $s^{-1}$. Moreover, T-$Nb_2O_5$@UTC demonstrates a higher capacitance contribution than T-$Nb_2O_5$, which should be attributed to the enhanced reaction kinetics induced by UTC modification and the 2D nanosheet structure (Figure 3g, h, i).

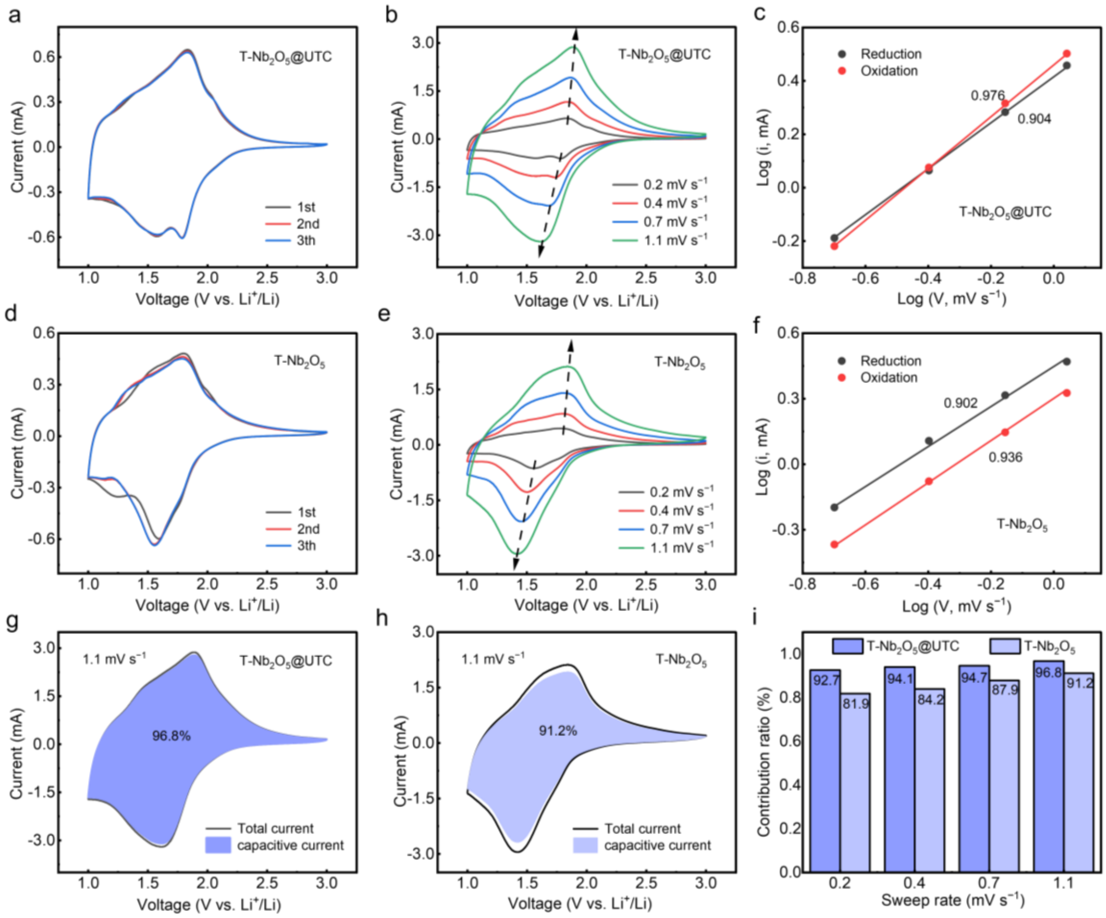

**Figure 3.** (**a**,**d**) CV curves of T-$Nb_2O_5$@UTC and T-$Nb_2O_5$ at 0.2 mV $s^{-1}$ over the first three cycles. (**b**,**e**) CV curves of T-$Nb_2O_5$@UTC and T-$Nb_2O_5$ at 0.2 to 1.1 mV $s^{-1}$. (**c**,**f**) The relationship between log $i_p$ and log $v$. (**g**,**h**) Pseudocapacitive contribution of T-$Nb_2O_5$@UTC and T-$Nb_2O_5$ at 1.1 mV $s^{-1}$. (**i**) Comparison of pseudocapacitive contributions for T-$Nb_2O_5$@UTC and T-$Nb_2O_5$ over the scan rates from 0.2 to 1.1 mV $s^{-1}$.

The electrochemical energy storage behavior of T-$Nb_2O_5$@UTC and T-$Nb_2O_5$ was investigated by galvanostatic charge/discharge (GCD) tests. T-$Nb_2O_5$ is used as the working electrode (WE) and a lithium sheet is used as the counter electrode (CE). The electrode loading is about 1.5 mg/$cm^2$. As shown in Figure 4a,b, the GCD curves of T-$Nb_2O_5$@UTC and T-$Nb_2O_5$ at different current densities have similar shapes, indicating excellent electrochemical reversibility. Furthermore, the distinct voltage plateau observed between 1.5–1.9 V corresponds to the reversible $Nb^{5+}$/$Nb^{4+}$ redox couple, as confirmed by CV analysis showing corresponding oxidation/reduction peaks. The rate performance data of T-$Nb_2O_5$@UTC and T-$Nb_2O_5$ were obtained through three independent experiments of the same batch (Figure 4c). The error bars represent the standard deviation of the three experiments (mean ± 5 mAh $g^{-1}$, n = 3), and the relative error is about 6% (Figure S3). The average discharge capacities of T-$Nb_2O_5$ at 0.1, 0.2, 0.5, 1, 2, and 5 A $g^{-1}$ are 179.6, 165.3, 149.2, 133.9, 112.1, and 62.9 mAh $g^{-1}$, respectively. In contrast, T-$Nb_2O_5$@UTC shows higher discharge capacities of 214.7, 202.4, 184.4, 168.0, 149.7, and 117.9 mAh $g^{-1}$ at the same current densities. When the current density is reduced back to 0.1 A $g^{-1}$ again, the discharge capacities of T-$Nb_2O_5$@UTC and T-$Nb_2O_5$ return to 213.2 and 166.5 mAh $g^{-1}$, respectively. Overall, T-$Nb_2O_5$@UTC exhibits superior rate performance and cycling stability. Benefiting from the synergistic effect of the 2D porous nanosheet structure and UTC coating, the rate performance of the T-$Nb_2O_5$@UTC anode surpasses that of most previously reported T-$Nb_2O_5$ materials (such as TT-$Nb_2O_5$@C, H-$Nb_2O_5$, T-$Nb_2O_5$, H-$Nb_2O_5$/rGO, etc.) (Figure 4d and Table S3) [10,16,42–46].

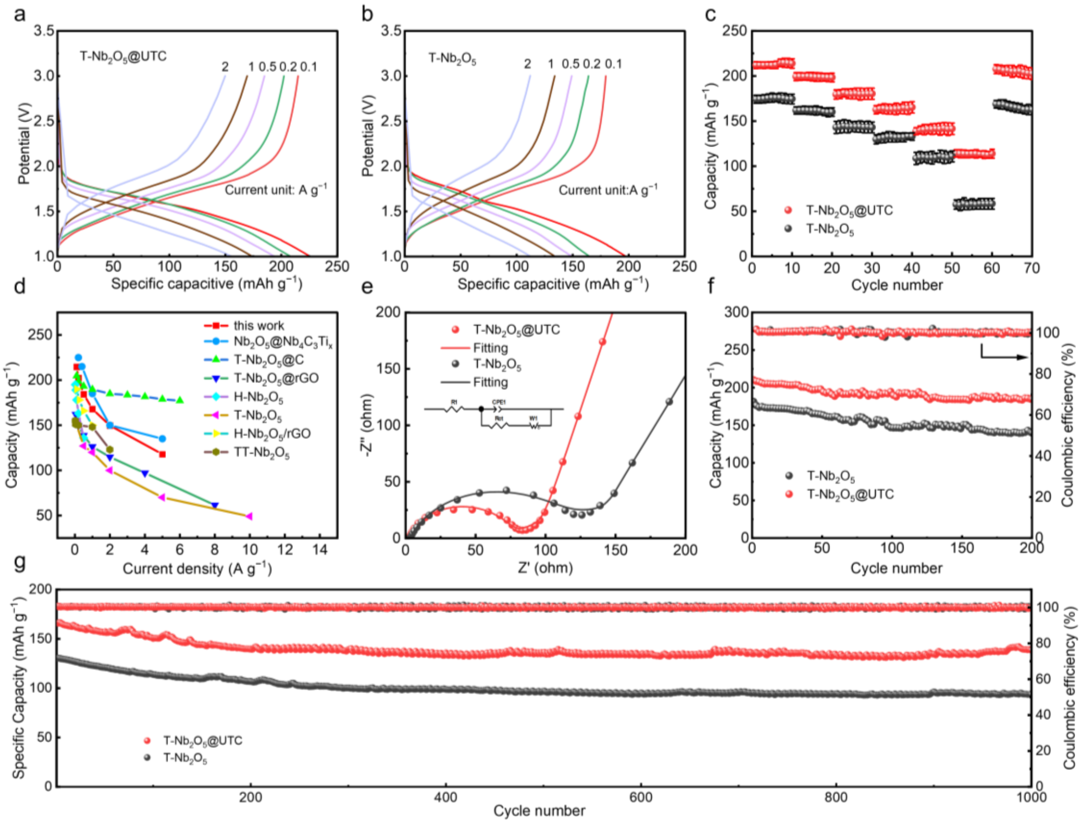

**Figure 4.** (**a**,**b**) GCD of T-$Nb_2O_5$@UTC and T-$Nb_2O_5$. (**c**) Rate performance of T-$Nb_2O_5$@UTC and T-$Nb_2O_5$. (**d**) Comparison of rate performance of different $Nb_2O_5$ electrodes. (**e**) EIS curves of T-$Nb_2O_5$@UTC and T-$Nb_2O_5$. (**f**) 200 cycles of T-$Nb_2O_5$@UTC and T-$Nb_2O_5$ at 0.1 A $g^{-1}$. (**g**) 1000 cycles of T-$Nb_2O_5$@UTC and T-$Nb_2O_5$ at 1 A $g^{-1}$.

Electrochemical impedance spectroscopy (EIS) measurements were conducted to investigate the charge transfer kinetics and interfacial properties of both T-$Nb_2O_5$@UTC and pristine T-$Nb_2O_5$ electrodes. In the Nyquist plot of EIS (Figure 4e), the first half of the curve typically appears as a semicircle, with its diameter representing the charge transfer resistance ($R_{ct}$) associated with the charge transfer process in the electrochemical reaction. The second half of the curve usually manifests as a straight line with a slope, corresponding to the Warburg impedance ($R_w$), which reflects the ion diffusion process in the electrolyte [47]. According to the equivalent circuit diagram fitting results, the $R_{ct}$ of T-$Nb_2O_5$@UTC is 83.4 Ω, significantly lower than that of T-$Nb_2O_5$ (128.3 Ω). Meanwhile, the $R_w$ of T-$Nb_2O_5$@UTC is also markedly lower than that of T-$Nb_2O_5$. This can be attributed to the structure of the 2D porous nanosheets and the coating of UTC, which effectively increases the contact area of T-$Nb_2O_5$@UTC with the electrolyte and reduces the interfacial resistance between them. Additionally, T-$Nb_2O_5$@UTC exhibits superior electrochemical stability, maintaining 87.9% of the initial specific capacity (184.8 mAh $g^{-1}$) after 200 cycles at 0.1 A $g^{-1}$ (Figure 4f). Even after 1000 cycles at 1 A $g^{-1}$, it still retains at 83.7% of the initial specific capacity (Figure 4g). In contrast, T-$Nb_2O_5$ maintains only 77.2% and 71.9% of the initial specific capacity at 0.1 and 1 A $g^{-1}$, respectively. The SEM images before and after 1000 cycles demonstrate that T-$Nb_2O_5$@UTC maintains its structural integrity (Figure S4), while T-Nb2O5 exhibits significant structural damage. This indicates that the UTC layer effectively alleviates the structural degradation of T-$Nb_2O_5$ caused by volume expansion and contraction during high-current cycling. In addition, the charge transfer resistance of T-$Nb_2O_5$@UTC does not increase significantly before and after cycling compared with T-$Nb_2O_5$ (Figure S5), which further suggests that UTC still maintains the structural stability of T-$Nb_2O_5$@UTC [48].

The lithium-ion diffusion behavior of T-$Nb_2O_5$@UTC and T-$Nb_2O_5$ was further examined using the galvanostatic intermittent titration technique (GITT) (Figure 5a, d). The diffusion coefficient ($D_{Li^+}$) of lithium ions in the electrode material can be calculated according to Formula (1) as follows:

$$D_{Li^+} = \frac{4}{\pi}\left(\frac{m_B\,V_m}{M_B\,A}\right)^2 \left(\frac{\Delta E_s}{\tau\left(\frac{dE_\tau}{d\sqrt{\tau}}\right)}\right)^2 \left(\tau \ll L^2/D_{Li^+}\right) \tag{1}$$

where $A$ represents the actual contact area of the electrode, Molar mass can be expressed as $M_B$, and $m_B$ denotes the mass of the active material. The symbol τ represents the current pulse time, $\Delta E_s$ represents the change in stable voltage, and the voltage change caused by the current pulse during the entire test can be expressed as $\Delta E_\tau$. Figure S6 illustrates that the single-step GITT consists of constant current and relaxation phases. Furthermore, the potential is proportional to $\tau^{0.5}$ (Figure 5b, e), simplifying the above in the form of Equation (2) as follows:

$$D_{Li^+} = \frac{4}{\pi\tau}\left(\frac{m_B V_m}{M_B A}\right)^2 \left(\frac{\Delta E_s}{\Delta E_\tau}\right)^2 \tag{2}$$

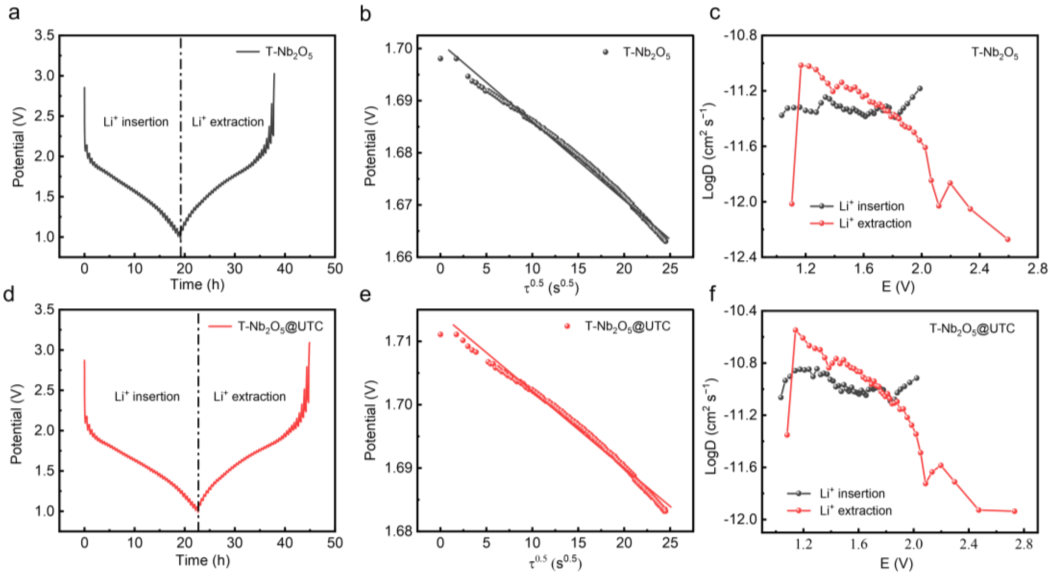

**Figure 5.** (**a**,**d**) GITT curves of T-$Nb_2O_5$@UTC and T-$Nb_2O_5$. (**b**,**e**) Linear relationship between $E$ and $t^{0.5}$. (**c**,**f**) $Li^+$ diffusion coefficient of the two samples.

Using the above formula, the average $D_{Li^+}$ values during lithium-ion insertion and extraction in T-$Nb_2O_5$ were calculated to be $4.72 \times 10^{-12}$ $cm^2$ $s^{-1}$ and $4.78 \times 10^{-12}$ $cm^2$ $s^{-1}$, respectively (Figure 5c). Under the same conditions, the average $D_{Li^+}$ values for T-$Nb_2O_5$@UTC are $1.07 \times 10^{-11}$ $cm^2$ $s^{-1}$ and $1.09 \times 10^{-11}$ $cm^2$ $s^{-1}$ (Figure 5f). Notably, the $D_{Li^+}$ of T-$Nb_2O_5$@UTC is about twice that of T-$Nb_2O_5$, indicating that UTC coating effectively enhances the lithium-ion diffusion capability. The enhanced lithium-ion diffusion kinetics of T-$Nb_2O_5$@UTC significantly optimize the concentration gradient of $Li^+$ at the electrolyte–electrode interface during high-rate electrochemical reactions. This improvement effectively reduces the concentration polarization and minimizes the overpotential related to $Li^+$ transport, thereby enhancing electrochemical energy storage performance.

## 3. Electrochemical Performance of Full Cells

To evaluate the practical application potential of T-$Nb_2O_5$@UTC, a T-$Nb_2O_5$@UTC||$LiFePO_4$ (T-$Nb_2O_5$@UTC||LFP) full cell was assembled.

As shown in Figure 6a, the Nyquist plot of the T-$Nb_2O_5$@UTC||LFP full cell shows the low $R_{ct}$ and $R_W$, indicating superior electrochemical reaction kinetics. The charge/discharge curves of T-$Nb_2O_5$@UTC||LFP exhibit voltage plateaus at 1.89 V and 3.5 V (Figure 6b), corresponding to the redox reactions of T-$Nb_2O_5$ and $LiFePO_4$, respectively. The discharge-specific capacities of T-$Nb_2O_5$@UTC||LFP were calculated to be 186.2, 147.8, 123.1, 105.6, 86.8, and 67.4 mAh $g^{-1}$ at 0.1, 0.2, 0.5, 1, 2, and 5 A $g^{-1}$, respectively. As shown in Figure 6c, when the current density is reduced back to 0.1 A $g^{-1}$, the discharge capacity of T-$Nb_2O_5$@UTC||LFP recovers to 177.6 mAh $g^{-1}$, indicating the superior rate performance of T-$Nb_2O_5$@UTC||LFP. In Figure S7, the assembled T-$Nb_2O_5$@UTC||LFP full cell successfully powered an LED panel, further highlighting its practical application potential. More importantly, the T-$Nb_2O_5$@UTC||LFP full battery exhibits excellent cycling stability, with the specific capacity decreasing by only 1.5% after 120 cycles at 0.1 A $g^{-1}$ (Figure 6d). Capacity decay may be attributed to the continuous thickening of the solid electrolyte interface (SEI) film on the negative electrode surface during battery cycling. The formation of the SEI film consumes active lithium and increases the internal resistance of the battery, leading to capacity degradation. Additionally, the cycling performance of T-$Nb_2O_5$@UTC||LFP at 1 A $g^{-1}$ was tested, as shown in Figure 6e. After 300 cycles, a capacity retention rate of 76.3% was maintained, demonstrating the favorable electrochemical stability of T-$Nb_2O_5$@UTC||LFP even at high rates.

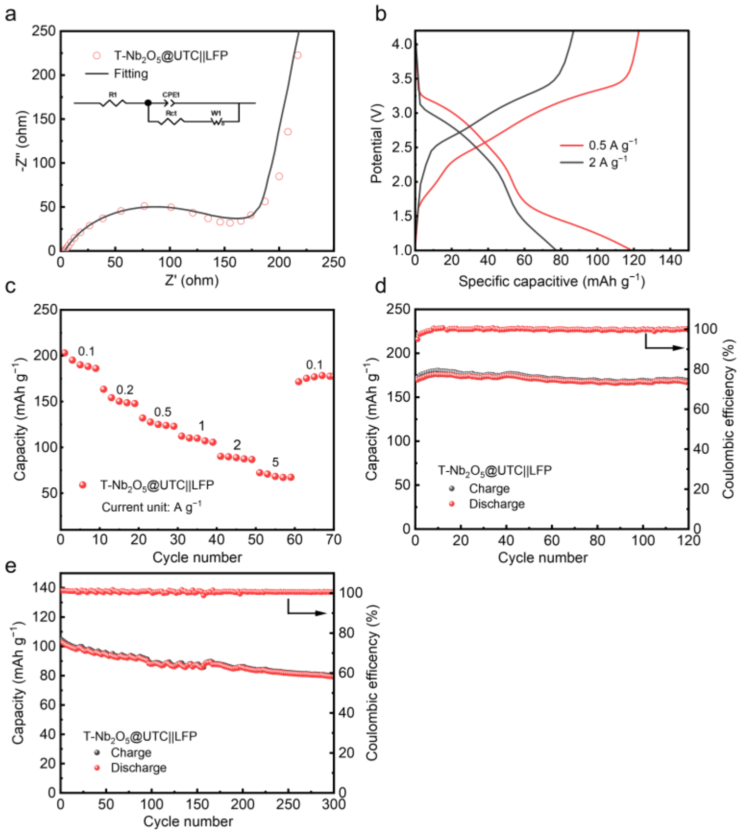

**Figure 6.** (**a**) Nyquist plot and equivalent circuit fitting of T-$Nb_2O_5$@UTC||LFP. (**b**) Charge and discharge curves of T-$Nb_2O_5$@UTC||LFP. (**c**). Rate performance of T-$Nb_2O_5$@UTC||LFP. (**d**) Cycle diagram of T-$Nb_2O_5$@UTC||LFP at 0.1 A g$^{-1}$ for 100 cycles. (**e**) Cycling diagram of T-$Nb_2O_5$@UTC||LFP after 300 cycles at 1 A g$^{-1}$.

## 4. Conclusions

In this work, we successfully prepared a two-dimensional T-$Nb_2O_5$ nanosheet decorated with an ultrathin carbon coating as a fast-charging LIB anode material. The porous nanosheet structure facilitates rapid lithium-ion transport through multiple channels, significantly shortening the ion migration distance. The ultrathin carbon layer, prepared via a facile acetylene pyrolysis process, further enhances the conductive network between primary particles while effectively mitigating particle fragmentation during long-term cycling. As a result, the T-$Nb_2O_5$@UTC demonstrates outstanding electrochemical performance in half-cell tests, achieving a capacitive contribution of 96.8% at a scan rate of 1.1 mV s$^{-1}$ and retaining approximately 87.9% of its initial capacity after 200 cycles at 0.1A g$^{-1}$. In full-cell tests, the T-$Nb_2O_5$@UTC||LFP delivers an impressive specific capacity of 186.2 mAh g$^{-1}$ at 0.1A g$^{-1}$, with a minimal decay rate of only 1.5% after 120 cycles. This exceptional performance is ascribed to the synergistic effect of its two-dimensional architecture and ultrathin carbon surface modification, offering valuable insights for the development of high-performance fast-charging LIB anodes.

**Supplementary Materials:** The following supporting information can be downloaded at: www.mdpi.com/xxx/s1. Figure S1. Refined spectra of T-$Nb_2O_5$@UTC and T-$Nb_2O_5$; Figure S2. Relationship between peak current and the square root of scanning speed $v^{1/2}$; Figure S3. Rate performance of T-$Nb_2O_5$ and T-$Nb_2O_5$@UTC obtained by three replicates of the same batch; Figure S4. SEM images of (a) T-$Nb_2O_5$ and (b) T-$Nb_2O_5$@UTC1000 after cycling; Figure S5. EIS comparison chart after 1000 cycles; Figure S6. A step in the GITT test of T-$Nb_2O_5$@UTC and T-$Nb_2O_5$ electrodes; Figure S7. LED lamp device display; Table S1. The properties of the as-obtained samples determined by nitrogen physisorption; Table S2. Element proportions obtained by XPS elemental analysis; Table S3. Electrochemical performance of several $Nb_2O_5$-based anode materials for lithium-ion batteries.

**Author Contributions:** Conceptualization, L.W. and G.W. (Gengping Wan); methodology, J.Z.; investigation, H.X. and C.D.; resources, H.Z.; writing—original draft preparation, H.X. and L.Y.; writing—review and editing, J.Z.; formal analysis, L.Y. and Y.Y.; project administration, G.W. (Gengping Wan); funding acquisition, G.W. (Guizhen Wang). All authors have read and agreed to the published version of the manuscript.

**Funding:** This work is supported by the National Natural Science Foundation of China (Grant Nos. 22168016, 22278101, 22068010, and 52365044), the Joint Fund for Regional Innovation and Development (Grant No. U24A20204), the Finance Science and Technology Project of Hainan Province (Grant No. ZDYF2025SHFZ018), the Innovation Project for Scientific and Technological Talents in Hainan Province (Grant No. KJRC2023C08), and the Fundamental Research Program of Shanxi Province (Grant No. 202303021211161).

**Institutional Review Board Statement:** Not applicable.

**Informed Consent Statement:** Not applicable.

**Data Availability Statement:** The data are included in this article and the supporting information.

**Conflicts of Interest:** The authors declare that they have no conflicts of interest.

## References

1. Liu, Y.; Zhu, Y.; Cui, Y. Challenges and opportunities towards fast-charging battery materials. *Nat. Energy.* **2019**, *4*, 540–550.
2. Li, S.; Wang, K.; Zhang, G.; Li, S.; Xu, Y.; Zhang, X.; Zhang, X.; Zheng, S.; Sun, X.; Ma, Y. Fast Charging Anode Materials for Lithium-Ion Batteries: Current Status and Perspectives. *Adv. Funct. Mater.* **2022**, *32*, 2200796.
3. Liu, Y.; Li, W.; Xia, Y. Recent Progress in Polyanionic Anode Materials for Li (Na)-Ion Batteries. *Electrochem. Energy Rev.* **2021**, *4*, 447–472.
4. Zhang, Y.; Chen, P.; Wang, Q.; Wang, Q.; Zhu, K.; Ye, K.; Wang, G.; Cao, D.; Yan, J.; Zhang, Q. High-Capacity and Kinetically Accelerated Lithium Storage in $MoO_3$ Enabled by Oxygen Vacancies and Heterostructure. *Adv. Energy Mater.* **2021**, *11*, 2101712.
5. Tang, Z.; Zhou, S.; Huang, Y.; Wang, H.; Zhang, R.; Wang, Q.; Sun, D.; Tang, Y.; Wang, H. Improving the Initial Coulombic Efficiency of Carbonaceous Materials for Li/Na-Ion Batteries: Origins, Solutions, and Perspectives. *Electrochem. Energy Rev.* **2023**, *6*, 8.
6. Wang, L.; Huang, F.; Zhu, G.; Dai, Z. $Nb_2O_5$ nanocrystals decorated graphene composites as anode materials for high-performance dual-ion batteries. *Nano Res.* **2024**, *17*, 1535–1541.
7. Wang, X.; Bai, Y.; He, R.; Yao, F.; Chang, L.; Nie, P. In situ construction T-$Nb_2O_5$ nanolayer on porous carbon cloth as Binder-Free anode for Lithium-Ion battery with long cycle life. *Appl. Surf. Sci.* **2024**, *670*, 160635.
8. Wang, R.; Wang, L.; Liu, R.; Li, X.; Wu, Y.; Ran, F. "Fast-Charging" Anode Materials for Lithium-Ion Batteries from Perspective of Ion Diffusion in Crystal Structure. *ACS Nano* **2024**, *18*, 2611–2648.
9. Shen, S.; Zhang, S.; Cao, X.; Deng, S.; Pan, G.; Liu, Q.; Wang, X.; Xia, X.; Tu, J. Popcorn-like niobium oxide with cloned hierarchical architecture as advanced anode for solid-state lithium ion batteries. *Energy Storage Mater.* **2020**, *25*, 695–701.
10. Griffith, K.J.; Forse, A.C.; Griffin, J.M.; Grey, C.P. High-Rate Intercalation without Nanostructuring in Metastable Nb2O5 Bronze Phases. *J. Am. Chem. Soc.* **2016**, *138*, 8888–8899.
11. Han, H.; Jacquet, Q.; Jiang, Z.; Sayed, F.N.; Jeon, J.-C.; Sharma, A.; Schankler, A.M.; Kakekhani, A.; Meyerheim, H.L.; Park, J.; et al. Li iontronics in single-crystalline T-$Nb_2O_5$ thin films with vertical ionic transport channels. *Nat. Mater.* **2023**, *22*, 1128–1135.
12. She, L.; Liu, D.; Zhao, Y.; Dong, L.; Wu, Z.; Xue, X.; Tian, Y.; Du, W.; Zheng, C.; He, S.; et al. Advances on Defect Engineering of Niobium Pentoxide for Electrochemical Energy Storage. *Small* **2025**, *21*, 2410211.
13. Shen, P.; Zhang, B.; Wang, Y.; Liu, X.; Yu, C.; Xu, T.; Mofarah, S.S.; Yu, Y.; Liu, Y.; Sun, H.; et al. Nanoscale niobium oxides anode for electrochemical lithium and sodium storage: A review of recent improvements. *J. Nanostruct. Chem.* **2021**, *11*, 33–68.
14. Ding, X.; Meng, F.; Zhou, Q.; Li, X.; Kuai, H.; Xiong, X. Complementary niobium-based heterostructure for ultrafast and durable lithium storage. *Nano Energy* **2024**, *121*, 109188.

15. Zheng, Y.; Chen, K.; Wang, L.; Chen, S.; Li, C. Pillaring Electronic Nano-Wires to Slice T-$Nb_2O_5$ Laminated Particles for Durable Lithium-Ion Batteries. *Small* **2024**, *20*, 2308727.
16. Zhang, H.; Wang, Y.; Liu, P.; Chou, S.L.; Wang, J.Z.; Liu, H.; Wang, G.; Zhao, H. Highly Ordered Single Crystalline Nanowire Array Assembled Three-Dimensional $Nb_3O_7(OH)$ and $Nb_2O_5$ Superstructures for Energy Storage and Conversion Applications. *ACS Nano* **2016**, *10*, 507–514.
17. Lian, Y.; Wang, D.; Hou, S.; Ban, C.; Zhao, J.; Zhang, H. Construction of T-$Nb_2O_5$ nanoparticles on/in N-doped carbon hollow tubes for Li-ion hybrid supercapacitors. *Electrochim. Acta* **2020**, *330*, 135204.
18. Zhang, X.; Zhu, K.; Xie, C.; Yang, P. Vertically implanting $MoSe_2$ nanosheets on superior thin C-doped g-C3N4 nanosheets towards interface-enhanced electrochemical activities. *Carbon* **2024**, *220*, 118884.
19. Mou, S.; Liu, S.; Dai, W.; Sun, Y.; Dong, F. Fluorine-induced D-band center shift in $Nb_2O_5$ nanosheets for efficient electrochemical formamide synthesis. *Appl. Catal. B Environ.* **2025**, *365*, 124963.
20. Cheon, S.; Lee, J.; Heo, J.; Im, J.; Cho, S.O. Nanoporous $Nb_2O_5$ with an Amorphous Structure for the Application as a Binder-Free Anode of a Hybrid Li-Ion Capacitor. *ACS Appl. Nano Mater.* **2024**, *7*, 23188–23195.
21. Wang, D.; Zhang, Z.; Zhang, D.; Zheng, Z.; Chen, G.; Zhang, N.; Liu, X.; Ma, R. Carbon coated $Nb_2O_5$ nanosheets via dopamine-induced phase transition for high-rate lithium-ion battery. *J. Power Sources* **2022**, *530*, 231274.
22. Li, Y.; Wang, Y.; Cui, G.; Zhu, T.; Zhang, J.; Yu, C.; Cui, J.; Wu, J.; Tan, H.H.; Zhang, Y.; et al. Carbon-Coated Self-Assembled Ultrathin T-$Nb_2O_5$ Nanosheets for High-Rate Lithium-Ion Storage with Superior Cycling Stability. *ACS Appl. Energy Mater.* **2020**, *3*, 12037–12045.
23. He, Z.; Zhang, C.; Zhu, Z.; Yu, Y.; Zheng, C.; Wei, F. Advances in Carbon Nanotubes and Carbon Coatings as Conductive Networks in Silicon-based Anodes. *Adv. Funct. Mater.* **2024**, *34*, 2408285.
24. Yu, J.; Yang, J.; Feng, X.; Jia, H.; Wang, J.; Lu, W. Uniform Carbon Coating on Silicon Nanoparticles by Dynamic CVD Process for Electrochemical Lithium Storage. *Ind. Eng. Chem. Res.* **2014**, *53*, 12697–12704.
25. Arya, A.K.; Raman, R.K.S.; Saxena, S. Multilayer CVD Graphene Coatings Developed with Suitable Geometrical Parameters for Improved Corrosion Resistance of Ni and a Ni–Cu Alloy in Chloride Environment. *Small* **2025**, *21*, 2405813.
26. Kim, J.; Cho, Y.-W.; Woo, S.-G.; Lee, J.-N.; Lee, G.-H. Advancements in Chemical Vapor Deposited Carbon Films for Secondary Battery Applications. *Small* **2025**, 2410570.
27. Liu, C.; Wang, B.; Song, Z.; Xiao, X.; Cao, Z.; Xiong, D.; Deng, W.; Hou, H.; Yang, Y.; Zou, G.; et al. Enabling Electron Delocalization by Conductor Heterostructure for Highly Reversible Sodium Storage. *Adv. Funct. Mater.* **2024**, *34*, 2312905.
28. Bhakar, A.; Taxak, M.; Rai, S.K.J.A.C. Significance of diffraction peak shapes in determining crystallite size distribution:A peak shape analysis procedure for pseudo-Voigt profiles and its application. *J. Appl. Crystallogr*. **2023**, *56*, 1466–1479.
29. Hu, J.; Li, J.; Wang, K.; Xia, H. Self-assembly $Nb_2O_5$ microsphere with hollow and carbon coated structure as high rate capability lithium-ion electrode materials. *Electrochim. Acta* **2020**, *331*, 135364.
30. Ali, A.; Chiang, Y.W.; Santos, R.M. X-ray Diffraction Techniques for Mineral Characterization: A Review for Engineers of the Fundamentals, Applications, and Research Directions. *Minerals* **2022**, *12*, 205.
31. Zheng, Y.; Yao, Z.; Shadike, Z.; Lei, M.; Liu, J.; Li, C. Defect-Concentration-Mediated T-$Nb_2O_5$ Anodes for Durable and Fast-Charging Li-Ion Batteries. *Adv. Funct. Mater.* **2022**, *32*, 2107060.
32. Li, T.; Huang, S.; Kane, N.; Wang, J.-H.; Luo, Z.; Zhang, W.; Nam, G.; Zhao, B.; Qi, Y.; Liu, M. Operando Raman and DFT Analysis of (De)lithiation in Fast-Charging, Shear-Phase H-$Nb_2O_5$. *ACS Energy Lett.* **2023**, *8*, 3131–3140.
33. Cao, X.; Pan, A.; Liu, S.; Zhou, J.; Li, S.; Cao, G.; Liu, J.; Liang, S. Chemical Synthesis of 3D Graphene-Like Cages for Sodium-Ion Batteries Applications. *Adv. Energy Mater.* **2017**, *7*, 1700797.
34. Zhao, G.; Zhang, L.; Li, C.; Huang, H.; Sun, X.; Sun, K. A practical Li ion battery anode material with high gravimetric/volumetric capacities based on T-$Nb_2O_5$/graphite composite. *Chem. Eng. J.* **2017**, *328*, 844–852.
35. Xu, X.; Robertson, S.J.; Yang, T.; Chen, F.; Geng, X.; Wang, Y.; Ji, F.; Sun, C.; Chen, S.; Shao, M.; et al. Interfacial space charge design with desired electron density to enhance sodium storage of $MoS_2$@$Nb_2O_5$ anode. *Nano Energy* **2024**, *127*, 109739.
36. Deng, S.; Zhu, H.; Wang, G.; Luo, M.; Shen, S.; Ai, C.; Yang, L.; Lin, S.; Zhang, Q.; Gu, L.; et al. Boosting fast energy storage by synergistic engineering of carbon and deficiency. *Nat. Commun*. **2020**, *11*, 132.
37. Wang, X.; Li, Q.; Zhang, L.; Hu, Z.; Yu, L.; Jiang, T.; Lu, C.; Yan, C.; Sun, J.; Liu, Z.J.A.M. Caging $Nb_2O_5$ nanowires in PECVD-derived graphene capsules toward bendable sodium-ion hybrid supercapacitors. *Adv. Mater*. **2018**, *30*, 1800963.
38. Zheng, Y.; Qiu, W.; Wang, L.; Liu, J.; Chen, S.; Li, C. Triple Conductive Wiring by Electron Doping, Chelation Coating and Electrochemical Conversion in Fluffy $Nb_2O_5$ Anodes for Fast-Charging Li-Ion Batteries. *Adv. Sci.* **2022**, *9*, 2202201.

39. Lotfabad, E.M.; Ding, J.; Cui, K.; Kohandehghan, A.; Kalisvaart, W.P.; Hazelton, M.; Mitlin, D.J.A.N. High-density sodium and lithium ion battery anodes from banana peels. *ACS Nano* **2014**, *8*, 7115–7129.
40. Mukherjee, R.; Krishnan, Lu, R.T.-M.; Koratkar, N. Nanostructured electrodes for high-power lithium ion batteries. *Nano Energy* **2012**, *1*, 518–533.
41. Shi, S.; Wang, G.; Wan, G.; Tang, Y.; Zhao, G.; Deng, Z.; Chai, J.; Wei, C.; Wang, G. Titanium niobate ($Ti_2Nb_{10}O_{29}$) anchored on nitrogen-doped carbon foams as flexible and self-supported anode for high-performance lithium ion batteries. *J. Colloid Interface Sci*. **2021**, *587*, 622–632.
42. Deng, B.; Lei, T.; Zhu, W.; Xiao, L.; Liu, J. In-Plane Assembled Orthorhombic $Nb_2O_5$ Nanorod Films with High-Rate $Li^+$ Intercalation for High-Performance Flexible Li-Ion Capacitors. *Adv. Funct. Mater*. **2018**, *28*, 1704330.
43. Meng, J.; He, Q.; Xu, L.; Zhang, X.; Liu, F.; Wang, X.; Li, Q.; Xu, X.; Zhang, G.; Niu, C.; et al. Identification of Phase Control of Carbon-Confined $Nb_2O_5$ Nanoparticles toward High-Performance Lithium Storage. *Adv. Energy Mater.* **2019**, *9*, 1802695.
44. Lübke, M.; Sumboja, A.; Johnson, I.D.; Brett, D.J.L.; Shearing, P.R.; Liu, Z.; Darr, J.A. High power nano-$Nb_2O_5$ negative electrodes for lithium-ion batteries. *Electrochim. Acta* **2016**, *192*, 363–369.
45. Li, S.; Wang, T.; Zhu, W.; Lian, J.; Huang, Y.; Yu, Y.-Y.; Qiu, J.; Zhao, Y.; Yong, Y.-C.; Li, H. Controllable synthesis of uniform mesoporous H-$Nb_2O_5$/rGO nanocomposites for advanced lithium ion hybrid supercapacitors. *J. Mater. Chem. A* **2019**, *7*, 693–703.
46. Pei, C.; Yin, Y.; Liao, X.; Xiong, F.; An, Q.; Jin, M.; Zhao, Y.; Mai, L. Structural properties and electrochemical performance of different polymorphs of $Nb_2O_5$ in magnesium-based batteries. *J. Energy Chem.* **2021**, *58*, 586–592.
47. Yu, M.; Liu, Y.; Wang, L.; Cui, F.; Liu, B.; Hu, W.; Lu, Y.; Zhu, G. Porphyrin-framed PAF Based Single-Ion Lithium Salt Boosting Quasi Solid-State Lithium-Ion Battery Performance at Low Temperatures. *Adv. Energy Mater.* **2024**, 2404008.
48. Ji, Q.; Xu, Z.; Gao, X.; Cheng, Y.-J.; Wan, X.; Zuo, X.; Chen, G.Z.; Hu, B.; Zhu, J.; Bruce, P.G.; et al. Carbon-emcoating architecture boosts lithium storage of $Nb_2O_5$. *Sci. China Mater.* **2021**, *64*, 1071–1086.